

Sputtered TiO₂ Nano Clusters as antireflection coating for Si Solar Cells

Master's Energy Science Thesis (University Utrecht)

Wingjohn Tang (Bsc)

Supervisor: dr. Frank Lenzenmann

Co-supervisor: dr. Pierpaolo Spinelli

Group: Solar Device Architecture

In collaboration with dr. Marcel Di Vece

(Nanophotonics, University Utrecht)



February 2015

Abstract

Antireflection (AR) coatings are a vital component in solar cells that allow them to efficiently harvest sunlight by reducing undesired reflection. Conventional coatings consist of a silicon nitride layer plus texturing approach, which is an effective solution that is often used in industrial crystalline solar cells. Next to the antireflection effect, the silicon nitride layer also provides needed surface passivation. However, in light of cost reductions and technological improvements, wafers get thinner such that texturing at a certain thickness can no longer be applied, making light trapping even more important. To tackle this, an alternative $\text{Al}_2\text{O}_3/\text{TiO}_2$ nano-patterned coating was proposed that uses a unique approach where the TiO_2 nano structures functions as Mie scatters, and in addition provides better passivation and antireflection characteristics.

This project explored the production of these TiO_2 Mie scatters through use of a nanocluster source. It was found through various techniques like scanning electron microscopy, UV-Vis-NIR spectroscopy and FDTD simulations that instead, a multilayer graded-index AR coating was made that achieved a broadband low reflectivity of 5.6% averaged over 300-980 nm in good accordance with theory. This was realized with a low refractive index porous TiO_2 layer, comprised of randomly stacked TiO_2 nanoclusters of about 20-25 nm. The work presented here sheds some light on a new AR coating that with more study could pave the way for cheaper and improved AR coating for solar PV.

Table of Contents

Abstract.....	2
1. Introduction.....	4
1.1. Background of Solar Cells.....	4
1.1. AR coating and Mie scattering theory.....	4
1.2. Research motivation.....	5
1.3. Goal and Scope.....	5
2. Methodology.....	7
2.1. Magnetron Sputtering with Nanocluster Source.....	7
2.2. Atomic Force Microscopy (AFM).....	9
2.3. Optical microscopy.....	9
2.4. Scanning Electron Microscopy (SEM).....	9
2.5. UV-Vis-NIR spectroscopy.....	10
2.6. FDTD Solutions simulations.....	11
2.7. SALSA sputtering set-up.....	12
3. Results & Discussion.....	13
3.1. Deposition results.....	13
3.2. Atomic Force Microscopy.....	14
3.3. Optical Microscopy.....	16
3.4. SEM.....	17
3.5. UV-Vis-NIR spectroscopy - reflection, transmission and absorbance spectra.....	18
3.6. FDTD simulations for reflection spectra.....	20
3.7. Discussion of Results.....	25
4. Conclusions.....	26
Acknowledgements.....	27
References.....	28

1. Introduction

1.1. Background of Solar Cells

Relying on the abundance of solar radiation on Earth, solar cells have changed dramatically over the decades since it was first introduced. Crystalline solar cells accounted for 90% of all solar cell production in 2013 with thin films 10%.¹ Briefly, a solar cell works by absorbing sunlight to create light-generated carriers (electrons-holes pairs), which are collected in an external circuit to do useful work for example, before returning back to the cell and recombining. Shockley and Quiesser calculated the theoretical limit of single-junction solar cells to be 33.7%.² There are numerous ways of losses with solar cells, starting with the sunlight that has energy which is less than the band gap of Si, electron-hole recombination without extraction, light reflection at the front of the surface, surface recombination or series resistance.

An example of a solar cell tackling multiple of loss pathways mentioned above are interdigitated back contact (IBC) solar cells (see figure 1.1-1). Conventional solar cells have top contacts to collect current, also known as “bus bars”. An IBC solar cell does not have these on the front, but only at the back. What it achieves is a low series resistance. No front contacts also means that design can better focus on light trapping and passivation at the front. It is considered a high efficiency crystalline solar cell that could have an efficiency over 20%.³

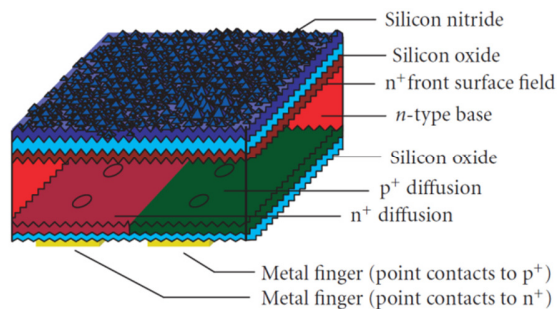


Figure 1.1-1: IBC solar cell

1.1. AR coating and Mie scattering theory

AR coating reduce reflection, and there are a number of ways to do that. The most common way is the application of silicon nitride and it also provides bulk passivation properties. The reason that nano structured dielectric Mie nano scatters can work as AR coating, is because light is preferentially scattered into one direction, i.e. that of into the wafer through leaky Mie resonances in the nano particles. By leaky Mie resonances it is meant that light is spatially momentarily trapped as it “bounces” or resonates inside the structures a few times before light is scattered into substrate. It was found that $\text{Al}_2\text{O}_3 / \text{TiO}_2$ AR Mie coating provides good surface passivation and good AR. The Mie nano structures were made by Substrate Conformal Imprinting Lithography (SCIL). A new technique that can create an array of TiO_2 nano pillars with high fidelity.⁴

1.2. Research motivation

Motivation for research on light trapping for solar cells has been in one way to find a new AR coating that beats conventional coatings in performance and costs, while still using cheap and abundant materials. Another reason to investigate is that solar cells will have Si wafers that are becoming increasingly thinner and at certain thinness, the conventional coating approach cannot be practically applied anymore while light trapping is still needed. The aim to improve the performance of solar cells by studying methods to create new AR coating will not only generate more scientific knowledge and open up new possibilities for study, but it will also address environmental and social problems. More specifically, better solar cells will become more attractive to implement as alternative renewable energy, and replacing conventional energy means through burning fossil fuel, due to their lowered costs per kWh of electricity. This reduces the negative impacts associated with global warming by reducing greenhouse gasses, increases the energy security of countries, and prevents depletion of abiotic resources.

1.3. Goal and Scope

The project aims to make a Mie AR coating that can be used for solar cells using a method that has not been done before, i.e. sputtering with the nanocluster (NC) source. To this end, structural and optical characterization of the AR coating will be executed using different techniques. Simulations will be done to validate and back results. Research and sub questions were formulated as follows:

Research question

Can we use the cluster source to deposit and obtain a nano structured layer of TiO_2 for use in solar cells with good antireflection properties such that the solar cell performance is similar to the Mie TiO_2 nano pillars made by SCIL?⁵

Sub Question

- Can we vary the experimental parameters (aggregation length, RF power, gas flow) such that the cluster source will yield clusters with the optimal parameters (pitch, width, height) for AR properties?
- What are the dimensions, morphology and pitch of the nanoclusters (NCs)? Atomic force microscopy (AFM) & scanning electron microscopy (SEM) will be used to answer this question?
- What are the optical properties (transmittance and reflectance) of the NCs? This will be determined by UV/Vis/NIR spectroscopy?
- How homogeneous is the sputtered layer of the NCs? Optical microscopy will determine this.

Structural information was attained by studying deposited NC of made samples with atomic force microscopy (AFM). Samples of interest were then examined in greater detail with scanning electron microscopy (SEM). Further optical characterization was done with optical microscopy and UV-Vis-NIR spectroscopy, to provide information that includes one important performance indicator for as use in solar cells. Finally, FDTD simulations were run to resolve whether the antireflection properties of the made AR coating are attributed to Mie scattering.

The layer of NCs is made by deposition on substrates using a nanocluster source based on the gas condensation technique, that uses sputtering and condensation to make spherical nanoparticles. Briefly, inert gas is introduced in the very low pressure environment of the machine, ionized, so can be directed

to strike a pure TiO_2 target, which liberates a plasma of TiO_2 atoms that then cool down and condense into clusters as they travel alongside a tube. A nozzle at the end of the tube produces a conical beam of NC that guide themselves towards a substrate.

2. Methodology

2.1. Magnetron Sputtering with Nanocluster Source

In short, sputtering is a physical deposition technique that involves knocking target atoms free out a solid target through collisions with ionized gas ions, with the purpose of coating a substrate with a thin film of the target material. By applying a DC voltage between the target and the substrate, and introducing an inert gas such Argon, which is commonly used, Ar ions are produced that strike the anode target. Ionization of the gas produces plasma that emits a characteristic light, also called a glow discharge (see Figure 2.1-1 (a)⁶). Secondary ions produced by the ionization of Ar, accelerate towards the substrate that can ionize more Ar gas. As sputtering creates a cloud of target atoms, these atoms diffuse through the aggregation zone before they land and condense on the substrate. This process happens in a low pressure environment and the plasma is rather diffuse, so the sputter rate is rather low. A pressure that is too high will lose target material to the wall due to diffusion. To increase the sputtering rate, magnetron sputtering was thought up as a solution. A magnet assembly behind the target creates magnetic field lines running near and into the target (see Figure 2.1-1 (b)). This traps electrons alongside the field lines, which has the effect of ionizing the plasma closer to the target and increases the Ar ion density. In addition to increasing the efficiency of sputtering, magnetron sputtering creates higher quality films due to less inclusion of impurities and less substrate damage due to electrons and ion bombardment.⁷ In a Nanocluster Source, which is based on the gas condensation method, sputtered target atoms in the aggregation region cool down through collisions with neutral Ar gas and water-cooled chamber walls. Small clusters begin forming after cooling as they nucleate and condense, which makes the clusters grow in size while traveling through the aggregation zone. A pressure difference drives the cluster through an aperture that then forms a cluster beam that are deposited on substrates.⁸ DC sputtering are used for conductive targets like metals for example. RF sputtering is used to sputter any nonconductive targets like ceramics and semiconductors.

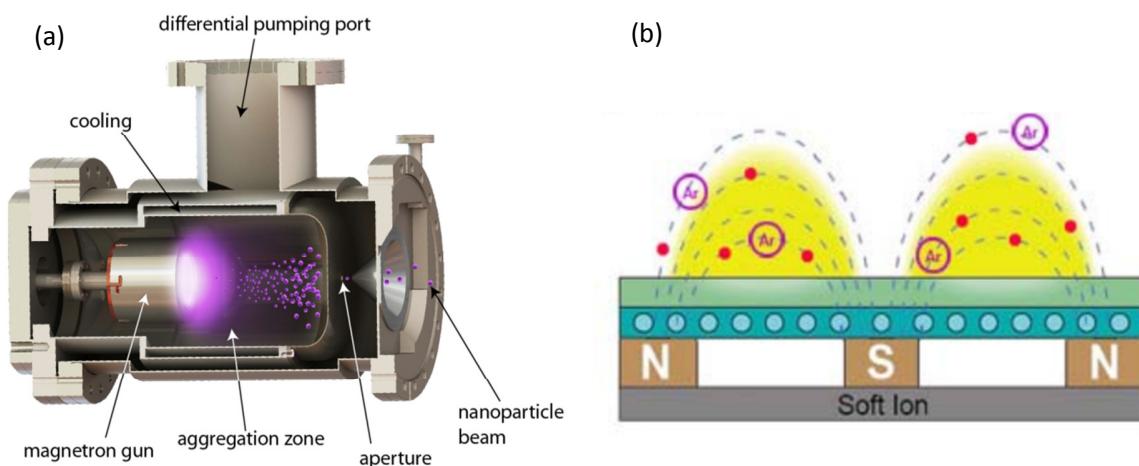


Figure 2.1-1 (a) Graphical representation showing the glow of the ionized gas that is used to sputter the target and the subsequent nucleation and growth of nano-particles that travel through the aggregation zone. Particles are forced through an aperture by a pressure difference and form a beam cluster (b) A magnetic assembly behind the target create specially shaped magnetic fields that trap electrons near the target surface, enhancing sputtering.

Set-up and pumps

A NC200U-B cluster source depicted in figure 2.1-2 (a) was operated for DC sputtering and the deposition of TiO_2 NC onto substrates in an adjacent central chamber to the right (barely seen). The magnetron gun holds a 2 inch diameter TiO_2 target, 6 mm thick, Model TRGT-TiO2-black, conductive, higher density and with a purity of 99.99%. Another chamber was used to load and unload samples shown in figure 2.1-2 (b)⁹. Samples are transferred from the loading chamber to the central chamber through a mechanically operated arm after opening the locks that separate the chambers. Turning the carousel slightly in the central chamber during a deposition of a substrate in front of the cluster beam allows for more homogeneous films. The Nanocluster (NC) source, central and load chamber each had its own turbo vacuum pump that should allow ultra-high vacuum (UHV) conditions. The background pressure was 1.4×10^{-5} and 6.0×10^{-9} mbar and the operating pressure about 1.3×10^{-4} mbar and 1.8×10^{-3} mbar during deposition of the central chamber and NC source, respectively. Also, the central and load chamber both use a secondary pump that is a VACUUBRAND diaphragm model MD-4 VARIO-SP pump. The NC source used a Pfeiffer rotary vane as a secondary pump.

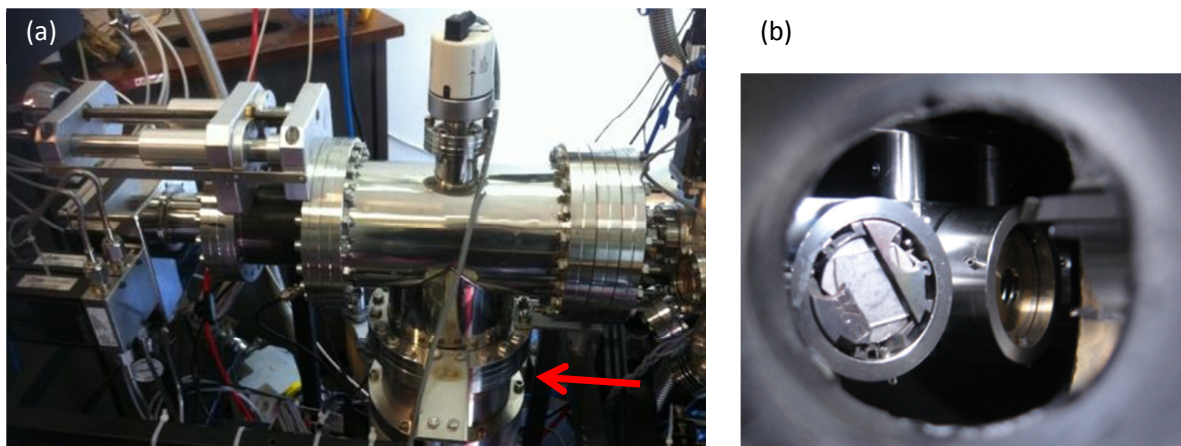


Figure 2.1-2 (a)The NC200U-B cluster source with turbo pump (pointed with arrow). (b) Inside look of the load chamber at the carousel with a sample holder inserted into one of its slots. The glass sample in this case is sandwiched between the holder and a metal plate.

Parameters

The cluster size of the NC source can be controlled with 3 parameters - the aggregation length (mm), the current (A), and the Ar gas flow (sccm). Using high currents and voltages, this will increase the sputtering rate. When this is combined with a high gas flow, and a long aggregation length it is possible to create large clusters.¹⁰ In this experimental set-up, a current as high as 0.22 ampere was used, but the voltage proved to be bottleneck when it went up to 400 V, which is the maximum. When this is occurred, a lower current had to be used due to the unstable plasma conditions. Aggregation length could be varied from 20 to 80mm, while the gas flow can go up to 20 sccm. The bottleneck for the gas flow is the turbo vacuum pump.

2.2. Atomic Force Microscopy (AFM)

AFM records a 3 dimensional image of a surface by scanning the surface of a sample with a sharp tip in a raster-like pattern. Tapping mode was used where the cantilever that is attached to the tip is oscillating at its resonant frequency. Keeping the tip-surface interaction constant is key to AFM, and so its oscillation amplitude must also be constant. The tip experiences a repulsive Van der Waals force when it approaches the surface closely during an oscillation (“tapping” the surface), and an attractive Van der Waals (VdW) force when it is further away. Consequently, the cantilever is deflected away from the surface for repulsive VdW forces, and deflected towards it for attractive VdW forces. A beam bounce method monitors this deflection by reflecting a laser off this cantilever onto a photodiode that is sensitive to the position off the laser spot. Any changes in this deflection are translated into height while scanning. A piezoelectric motor allows the scan movement of the probe.¹¹

A MultiMode Scanning Probe Microscope was used in conjunction with the Digital Instruments Nanoscope IIIa SPM controller shown in figure 2.2-1 (a)-(b). Figure (a) shows the microscope made of the optical head, which houses the piezoelectric motors, probe, photodiode and laser. The scanner facilitates the loading and unloading of the sample. The base allows AFMs operators to read the LCD display that is necessary to align the laser on the end of the cantilever prior to scanning. Bruker OTESPA AFM probes were used.¹²

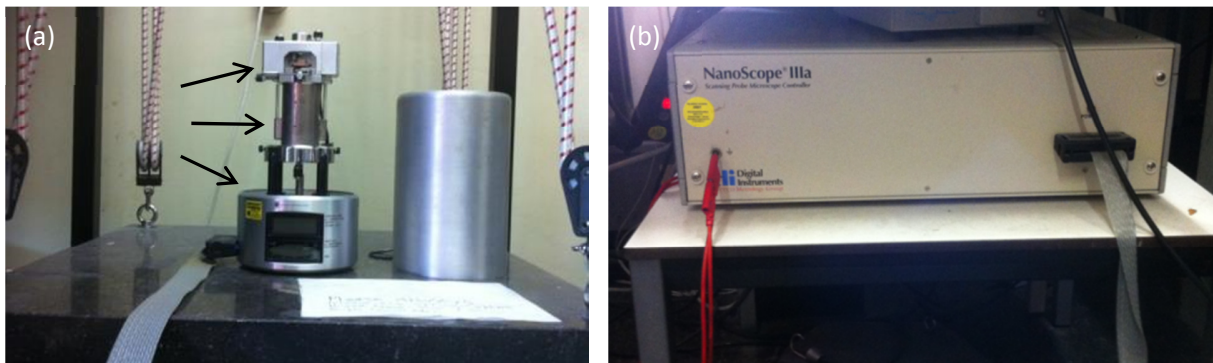


Figure 2.2-1 (a) Microscope used to record AFM micrographs. The three arrows (from top to bottom) indicate the optical head, scanner and base. Lift depicted is not used. (b) Nanoscope IIIa SPM Controller

2.3. Optical microscopy

A Leica optical microscope was used to study the samples at magnifications from 37.5 to 1500x magnification. The microscope model is a MEF4M, an inverted metallograph that has digital imaging capturing and software, analySIS auto 5.0 that allows image analysis. The microscope allows samples to be placed on top in an inverted position.

2.4. Scanning Electron Microscopy (SEM)

SEM works on the principle of a focused electron beam that is scanned over the surface of interest in a raster like pattern, while operating in ultra-high vacuum (UHV). The beam size is controlled by multiple electromagnetic lenses and can focus the beam on the sample. The energy of the electrons is determined by the accelerating voltage, as they will travel faster towards the sample with a higher

voltage. The electron beam excites atoms by hitting them, after which they emit secondary electrons and are picked up by detectors. The signal is then translated to a greyscale image that allows interpretation of the topographic information. A Hitachi SU-70 microscope was used to take high-resolution images of the sample, which allows accelerating voltages from 0.5-30 kV and magnifications of several 100k times, although the latter was limited by charging on the examined samples, which caused artefacts in micrographs.^{13 14}

2.5. UV-Vis-NIR spectroscopy

Traditional UV-Vis spectroscopy cover measuring the absorption of light over a range of wavelength that is shined through a clear, or translucent solid or liquid, by looking at the transmitted light that was not absorbed by the sample. Reflection of light can also occur for opaque or reflecting surfaces, and measuring that light requires a diffuse reflectance accessory. Reflection is a sum of two components, namely specular and diffuse reflectance (see figure Figure 2.5-1). Diffuse reflectance is responsible for the dull-looking surfaces, while the mirror-like surfaces are associated with specular reflectance. The accessory used to measure the total and diffuse reflectance is usually an integrating sphere, which is a hollow sphere with a diameter of 150 mm and the inside walls are covered with a highly diffuse reflectance coating. A transmission port allows a sample beam to enter the sphere and hits the sample surface at a theta angle of 8 degrees. For diffuse reflectance measurements, a 'gloss trap' is used. It is a special black cover put over the specular exclusion port to absorb the specular reflected light. For total reflection measurements, the black cover is replaced with one that has the same coating that of the inner wall of the sphere.

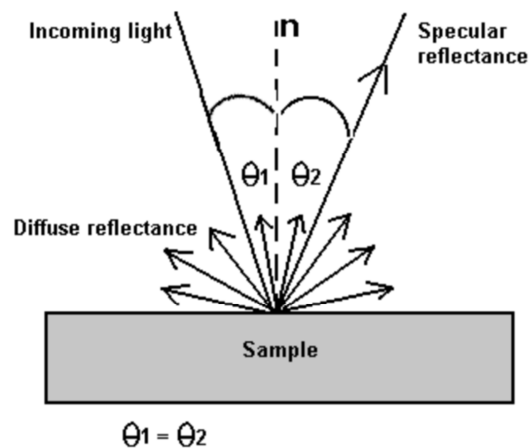


Figure 2.5-1 Diffuse and specular reflectance with respect to incoming light. The normal is also drawn to illustrate that the theta angle one is equal to that of two.

Varying between 0 and 1, absorbance (A) is defined as follows:

$$A = 1 - R - T$$

Equation 2.5-1

Where T is transmission and R is total reflectance (sum of diffuse and specular reflectance).

Equipment

A Cary 5000 series was used to record total and diffuse reflectance of measured samples in the wavelength range of 300 to 1200nm. An external Varian 1800 Diffuse Reflectance Accessory (DRA) is fitted in the sample compartment of the instrument. A small spot kit is installed prior to measurement, which reduced the beam size fit for the sample size. A certified reflectance (CRT) (number 8145) standard made of PTFE covered the sample port and a baseline is recorded (full reflectance). Prior to recording, a second cover is put over it to block stray light from entering the sample port. Then, the CRT standard is removed and another baseline is recorded (0 reflectance). Having done this, the samples could be placed against the sample port and either a diffuse or total reflectance spectra could be recorded.

For recording the transmission, the CRT standard was placed against the sample port. A sample holder was placed in front of the integrating sphere, and the baseline was recorded (full transmission). Finally, the sample was placed in the sample holder and the transmission spectra could be recorded.¹⁵

2.6. FDTD Solutions simulations

Maxwell's equations describe how electric and magnetic fields behave and how they interact with physical matter. These are the equations that are used to get to a solution in FDTD simulation. The method treats space and time discrete. Space is described as a very fine mesh comprised of a basic unit, called the Yee cell, and is smaller than the wavelength of light (see Figure 2.6-1).¹⁶ The time it takes for the electromagnetic fields to step into a neighbouring cell is equal one discrete step in time. However, the electric and magnetic fields have different positions in the cell, such that the method require the electric field values to be computed first, and then those of the magnetic field, before computing the next electromagnetic field values one time step further, respectively. In other words, there is half a discrete step in time and space difference between the electric and magnetic fields.

By changing the equations in the cell edges, a continuous network of cell edge can form a material of choice, and enough cells can produce good approximations to geometrical structures. Also, unless a material is added, all cells are otherwise considered to be free space.¹⁷

Lumerical FDTD Solutions 8.11.318 software¹⁸ was used to run the simulations. The tabulated n,k values of TiO₂ (amorphous) was added to the material database of the software.¹⁹ The number of cells in a simulation is correlated to the time, accuracy and computer resources necessary to complete.

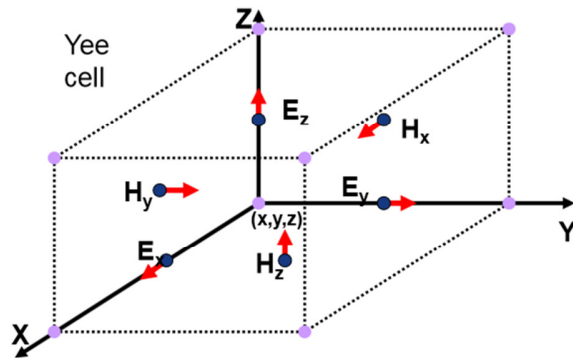


Figure 2.6-1 Yee cell with the magnetic field vectors located on the faces of the cell, and the electric field vectors located on the axes.

2.7. SALSA sputtering set-up

A sputtering set-up (DC) was also used to deposit TiO_2 on a wafer (250 watt, 20 sccm Ar with few % of O_2 , background pressure was 5 μbar .) for 45 minutes to determine the deposition rate with a Veeco Dektak 8 surface profilometer. A deposition time of 35 minutes was then done on 3 Si wafers (mechanically polished, Al_2O_3 passivated) to get a TiO_2 layer with a thickness of 50 nm.

3. Results & Discussion

3.1. Deposition results

TiO₂ cluster depositions were primarily performed on polished Si wafers (no passivation) with a thin layer TiO₂ of about 50nm, as measured with spectroscopic ellipsometry. The layer was prepared by electron beam evaporation. DC sputtering with the NC source and a conductive TiO₂ target was repeated a number of times find the right settings (aggregation length, Ar gas flow, current) for making clusters with the right parameters (pitch = 500 nm width = 350 nm and height = 100 nm²⁰). The substrates were cut in into pieces of about 1 x 1 cm in size with a diamond pen prior to deposition. The angle of incidence of the incoming clusters on the substrate was changed every 2 minutes. At an angle of 0, ~15, and ~30 degrees, the total deposition time was 2, 4, and 4 minutes in total, respectively. This is done to create a more homogeneous layer due to the inhomogeneous cluster beam.

Table 3.1-1 shows the parameters were that were used to create a sample of interest (see figure 3.1-1). The left and right side (purple color) of this sample shows the ~50nm TiO₂ layer. Aside from this, two small areas of a lighter blue at the edges lie adjacent to the centre part. These areas correspond to TiO₂ nano pillars made by SCIL that were already there before the deposition and will not be focused on. More importantly, the centre part of the substrate shows the deposited layer (dark blue). Comparing the colour of the layer with that of the substrate below shows the reflectivity of the substrate has been reduced, which is a first indication of the AR properties of the TiO₂ NCs. This layer will be the main point of discussion of this thesis. Whether this can be ascribed to Mie scattering or not will be discussed in the following subchapters.

Sample number	Ampere (A)	Voltage (V)	Aggregation Length (mm)	Ar Gas Flow (sccm)	Time (minute)
CS707	0.22	345	40	15	10

Table 3.1-2 Parameters used for the DC sputtering with the Cluster Source set-up.

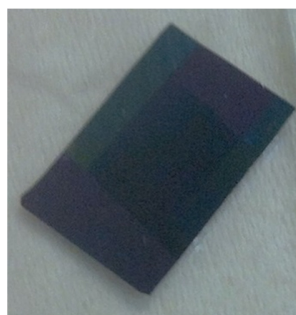


Figure 3.1-1 CS707: A Si wafer with a 50nm TiO₂ (purple) layer, and at the center the deposited layer of TiO₂ nano clusters (dark blue).

3.2. Atomic Force Microscopy

AFM was used to find and characterise the nano particles after sputter depositions. The micrograph in figure 3.2-1 was taken of a reference, a TiO₂ layer stacked a Si wafer. A “flatten” filter was used to remove any “tilt” or “bow” effect in all micrographs, that arises due to the curved motion of the scanner head while scanning. This was also taken from the same batch of wafer that was used as the substrate the sample of interest in the previous section. Two important observations are made from the figures. Firstly, the surface is not atomically flat, with troughs that varying from about 40 to 100 nm in depth. Secondly, the surface already shows a finer texture, with features that typically range from about 10 to 20 nm in size.

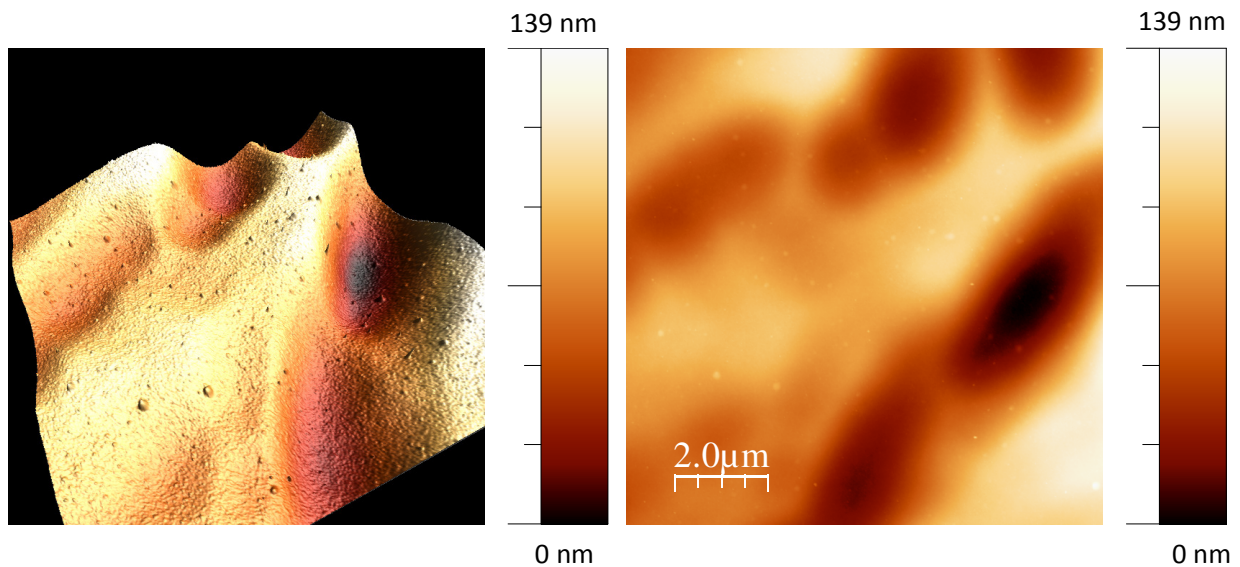


Figure 3.2-1 Micrograph of a reference Si wafer with TiO₂ layer 3D (left) and 2D representation (right).

Figure 3.2-2 depicts one of the micrographs made of the deposited layer of NC shown in figure 3.1-2. Tall, features are seen ranging from 60 to 170nm in height and densely populate the surface. The areas where the troughs are situated similar to those seen in the reference can also be distinguished by its rough dark outline. The average height of this layer was determined by using the profile function of software to measure the height of each individual round-like feature, and was repeated at least 50 times. The resulting histogram is shown in figure 3.2-3. The average height was calculated to be 110.6 nm, and the standard deviation 23.2 nm.

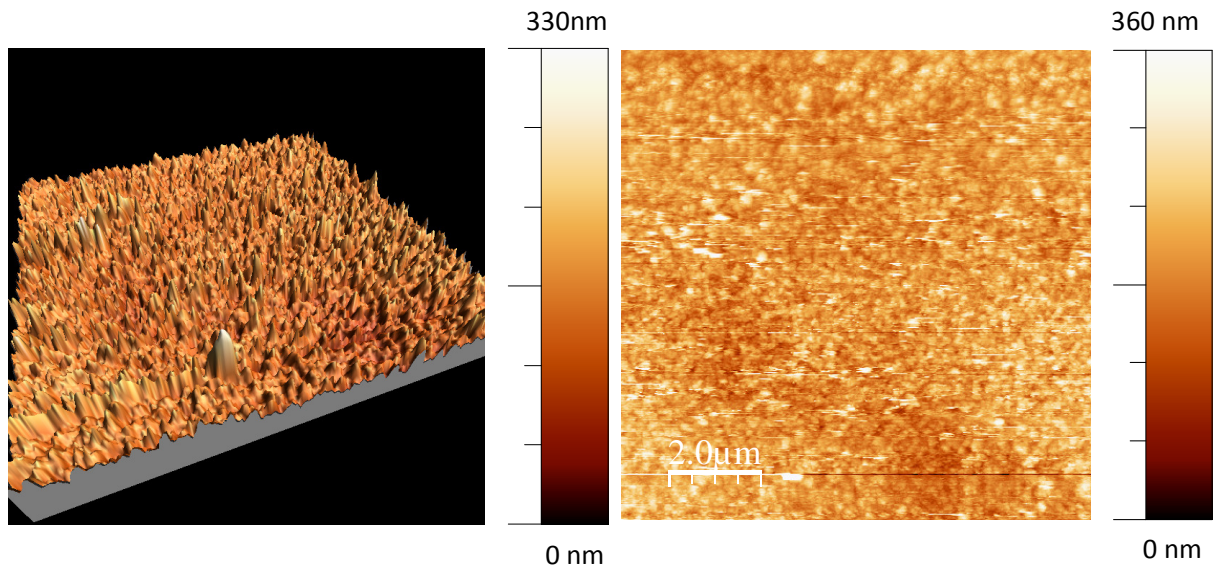


Figure 3.2-2 Micrograph of nano cluster that were deposited on the TiO₂ substrate (CS707), 3D (left) and 2D (right).

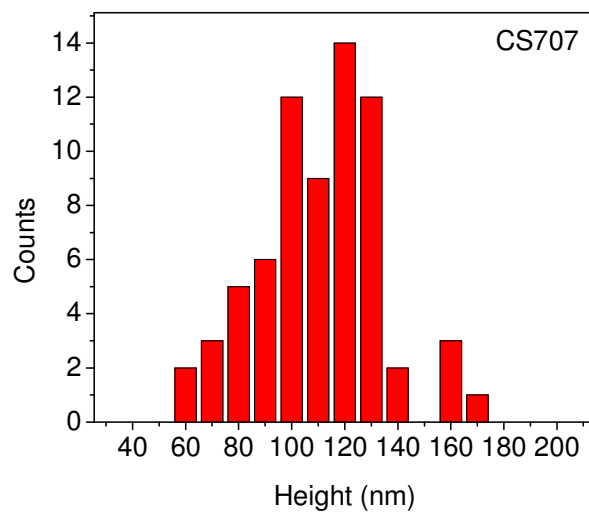


Figure 3.2-3) Histogram of the number of counts versus the height of the measured feature.

3.3. Optical Microscopy

An optical microscope was used to study the layer of NC at different magnifications. Figure 3.3-1 shows two images captured at different positions with a magnification of 37.5. Figure (a) depicts not only the layer of NC, but also the TiO₂ layer and nano pillars with sharply-defined interfaces separating them. Almost the entirety of figure (b) depicts the section covered with NC (the small left and right bottom corner are not part of it). Two distinct, separate regions of the nano clusters can be identified in this image; the left side in blue (Region A) and right side in purple (Region B). While the transition between the two regions is gradual, the regions themselves are quite homogeneous. The reason for there being 2 different regions, which from now on will be addressed as region A and B, respectively, will be given a detailed analysis later on. It has to do with their difference in refractive index.

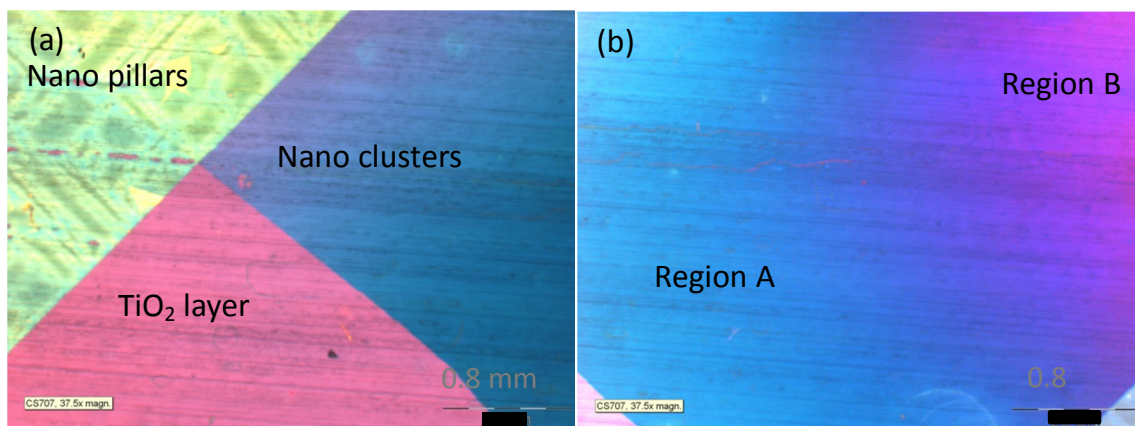


Figure 3.3-1 Light Microscopy images taken at 37.5 times magnification. 3 distinct, sharp regions can be identified in (a) going clockwise starting from the bottom; TiO₂ layer, nano pillars, and NC. (b) Two separate regions (A and B) can be seen for the layer of NC.

Figure 3.3-2 (a) was taken at the highest magnification of the light microscope, 1500 times. Individual nano pillars can now be discerned, which is most clearly seen in figure (b). Each particle has a diameter of about 300 nm. When this is compared to layer of NC, no lateral features can be made out, which suggests that the particle sizes fall under the limit of the resolving power of the optical microscope.

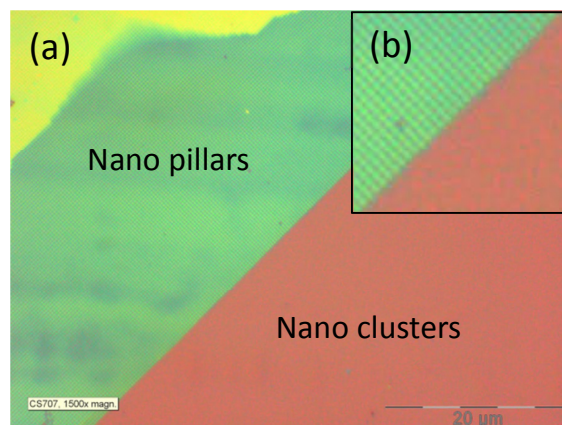


Figure 3.3-2 (a) Image taken at 1500 times magnification near the interface of the nano pillars and nano clusters. (b) gives a closer view on a small section of the interface.

The thickness of the Si wafer was also determined with optical microscopy by holding the wafer in an upright position, so that its smallest side is orthogonal to the light beam. Knowing the thickness, we know the absorption of the wafer. The result is shown in figure 3.3-3. An average value of 156.6 μm was found with a standard deviation of 3.6 μm . An assessment of the morphology for the NC can be made with the SEM technique, which is given in the next subchapter.

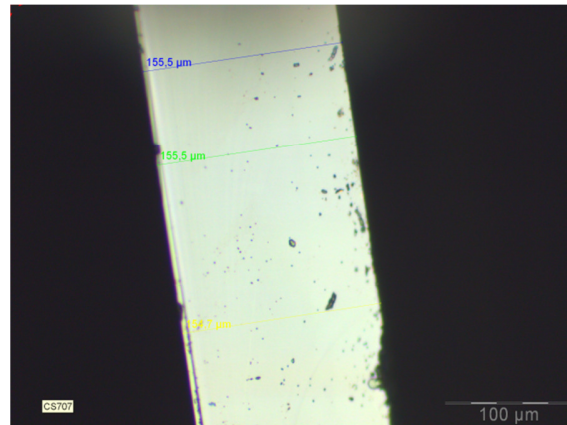


Figure 3.3-3) Cross-section of Silicon wafer and measured thickness.

3.4. SEM

The result of the SEM on the nano clusters is shown in figure 3.4-1, which was taken at a magnification of 1×10^6 times. The image shows that the NCs are randomly packed, with uniform size between about 20-25nm. Also, the particles can be observed to partly coalesce forming structures marked with a red circle. Importantly, the image shows that the sputtered NCs, despite coalescing into bigger structures, do not form an array of Mie scatterers with the optimal dimensions of 100 nm in height, 500 nm pitch, and 350 nm in width, which is are desired for a Mie-based ARC.. This is one indication that the anti-reflection effect observed visually in fig. 3.1.1 is not attributable to Mie resonance as the particles are too small for Mie scattering in the visible spectral range. The clusters do not seem to stack efficiently forming well-defined bigger nanoparticles, but instead the structure as a whole seems a porous material that is a mixture of air and TiO_2 .

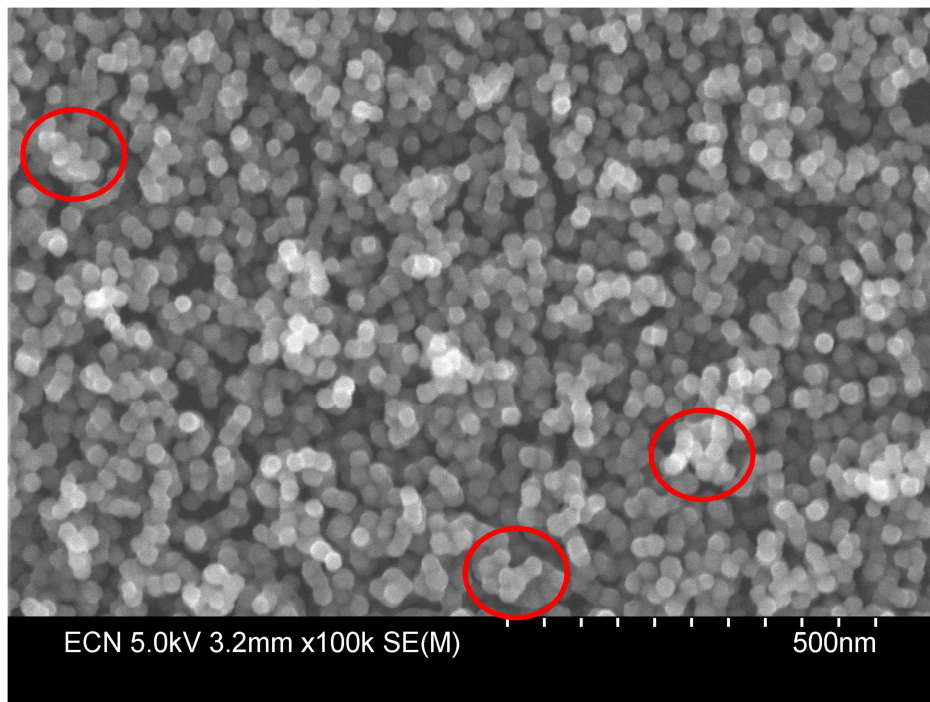


Figure 3.4-1 SEM micrograph of TiO_2 nanoclusters, which randomly pack in what results in a porous layer. Indicated in red circles are agglomerates of partly fused nano clusters.

3.5. UV-Vis-NIR spectroscopy - reflection, transmission and absorbance spectra

The total and diffuse reflectance of the sample with NC, and the reference Si wafer with a TiO_2 layer, were measured in a UV-VIS-NIR integrating sphere setup. The results are shown in figure 3.5-1 three total reflectance measurements were taken of the reference, with each time a slightly different position, so that the averaged spectra can be calculated. This was also done for the NC layer; one measurement that was taken on region B of the NC layer, and two measurements on region A. As can be seen for the data, the effect of the NC layer is a significantly lowered reflectance over the entire investigated range (300-1200 nm), with the measurements showing region A achieving a lower reflectance than region B. The sudden increase in reflectivity occurring at a wavelength of 980 nm is attributed to light that reflected from the back side of the Si wafer and not absorbed in the wafer. Due to this effect, the AR properties of the NC coating can be studied only in the 300-980 nm spectral range. On average, the total average reflection was brought down to 5.7% on region A in the range of 300-980nm from about 16% for the reference. For comparison, an $\text{Al}_2\text{O}_3/\text{TiO}_2$ nano pillar Mie coating was found to have an average reflection of 2.6% over 420-980 nm range.²¹

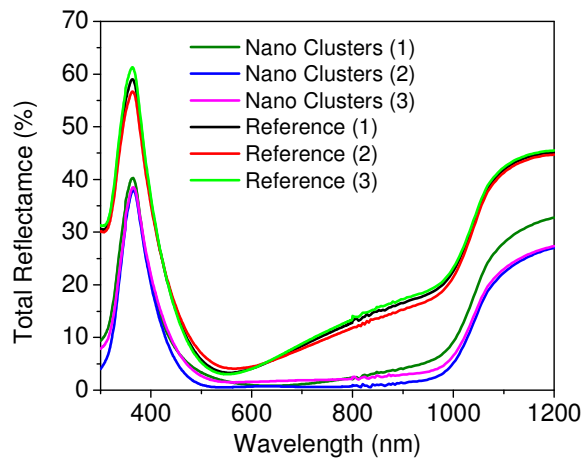


Figure 3.5-1 Total Reflectance measurements of a Si wafer with $\text{TiO}_2+\text{TiO}_2$ NC, and the reference, which is a Si wafer with TiO_2 layer.

The transmission was measured of the sample and reference which is depicted in the left graph in Figure 3.5-2. No transmission reduction was seen for the NC compared to the reference. This shows that, while providing excellent AR properties, the sputtered NC array does not provide an effective light trapping mechanism. Light is efficiently coupled into the wafer, but not scattered at angles large enough to provide light trapping via total internal reflection. This is another indication that the reduced reflection is not due to Mie resonances that scatters light into the wafer.

Based on the measured reflection and transmission, the absorbance was calculated according to equation 2.5-1, and is shown in the right graph. The absorption enhancement is mainly due to the broadband decrease of specular reflectance.

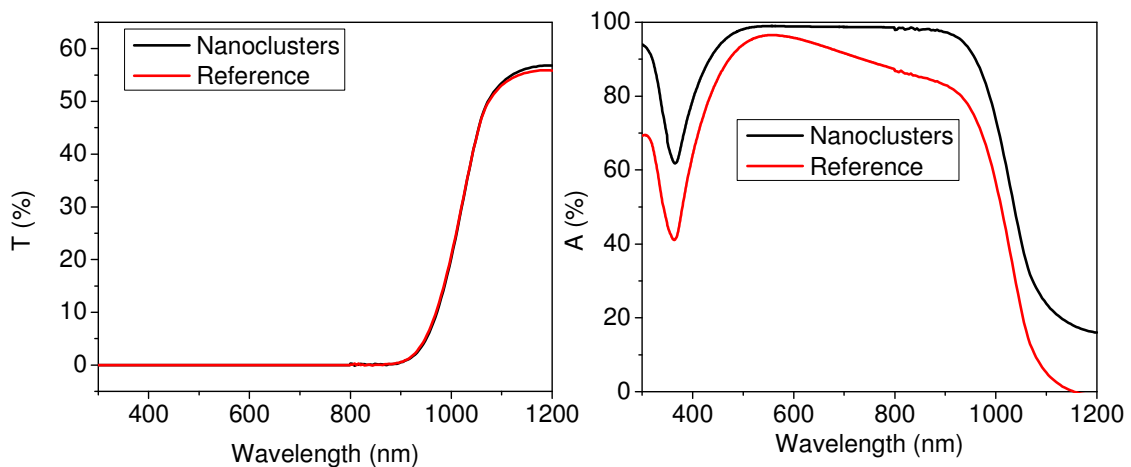


Figure 3.5-2 Transmission measurements for the nanoclusters and the reference (Nanocl. T & Ref T) without a layer of TiO_2 nano clusters. Also shown is the calculated absorbance of the nanoclusters based on the transmission and reflectance spectra

As we already saw with SEM, the voids between the particles are typically smaller than the wavelength of light. That means that light that travels through this medium experiences an effective refractive index in between that of air and TiO₂. The mechanism behind the AR effect is thus likely due to be a combination of the flat TiO₂ layer and porous TiO₂ layer, with an effective index which is in-between that of air and TiO₂. The system is thus equivalent to a double layer ARC. To prove this theory, in the next subchapter we use FDTD simulations to reproduce the reflection spectra and to find the effective refractive index of the NC layer.

3.6. FDTD simulations for reflection spectra

The following FDTD simulation set-up was used to run the calculations (see Figure 3.6-1). Firstly, the FDTD box had a box size of 0.3x0.3x4.3 μm, and periodic boundary conditions for the x and y. A PML boundary condition (perfectly matched layer) was used for the z, which runs orthogonal to the direction of the light source. This layer ensures that all light will be absorbed, and will not be reflected back. A plane wave source was used to inject light alongside the plane of the source. The monitor was placed above the source, recording the output power from 300-1200 nm with 200 data points. Also, a mesh accuracy of 2 was used for fast simulations. A convergence test was done to prove that a mesh accuracy 2 does not yield artifacts compared to higher mesh accuracies.

The simulation setup consists of 2 layers stacked on top of each other - a 150 nm thick Si layer at the bottom, and a TiO₂ layer with a thickness that was varied between 30 and 60 nm for each different simulation. The Si thickness found in chapter 3.3 was 156.6 μm, but this was not used in the simulations due to hardware limitations. However, PML boundary conditions were used to simulate a very thick Si layer. Simulations were run with a 1 μm thick layer of Si, and the resulting reflection spectra did not differ that from the simulation where a thickness of 150 nm thickness was used. Since the exact thickness of the TiO₂ is not known, but was estimated at about 50 nm, simulations were run to determine the thickness that best corresponded to the experimental results of the reference sample by varying the thickness between 30 and 60 nm. The results of this are shown in Figure 3.6-2 Simulated reflection spectra (dashed lines) plotted next to the ones measured experimentally (solid lines) for both figures. (a) The thickness of the TiO₂ layer stacked on Si was varied and compared to the experiments to determine the best matching thickness (55nm) and then was used as input for the simulations in figure (b). Figure 3.6-2a, where the reflectance of the reference is found by simulations (dashed lines), and are compared to the ones that were experimentally determined (solid lines). The TiO₂ thickness of 55 nm has a good agreement with the experiments below 1000 nm. Above 1000 nm, the experiments show a comparatively higher fraction of reflected light. This is explained by the indirect bandgap of Si, which causes the red light of this part of the spectrum to be not fully absorbed by the wafer and is reflected off the backside of the Si. In the simulations, light is absorbed by the PML layer, which explains the discrepancy.

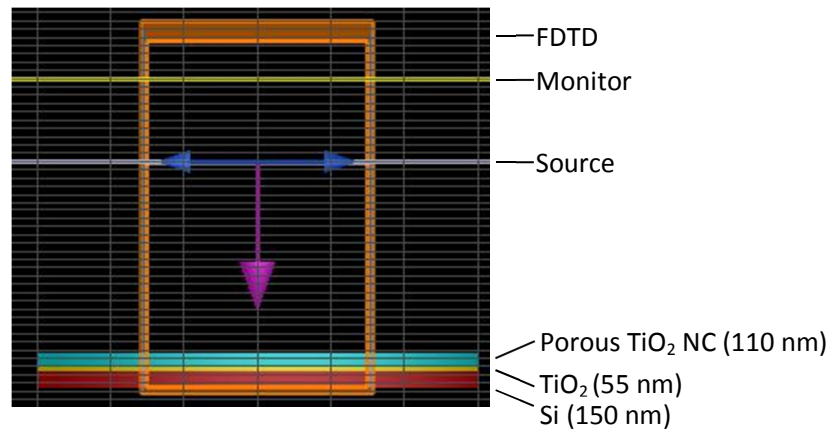


Figure 3.6-1 FDTD set-up simulation. Simulations were run first run without the layer that approximated the NC layer (only TiO₂ and Si), so that the best experimentally agreeable thickness for the TiO₂ was found. This was then used as input for further simulations including the approximated NC layer.

Next, the TiO₂ thickness that best matched the experiment reflection spectra was then used as input for further simulations, where a dielectric layer was added on top of the TiO₂ layer. The added layer represents the porous layer of NC, and the average thickness of the layer was set to 110 nm, which was determined with AFM (see chapter 3.2). Then, the refractive index of the layer was varied between 1.2 and 1.7 with 0.1 incremental steps, and the reflection spectrum calculated for each index. The results are shown in Figure 3.6-2 (b) (dashed lines). These were compared to the experimental reflection spectra measured of region A (Nanoclusters (1)), and that of region B (Nanoclusters (2)). When these are compared to the simulations it is concluded is that the simulated reflectivities obtained for a refractive index of 1.3 and 1.4 agree well in the spectral range below 1000 nm with the experimental measurements on region B and A, respectively. For wavelengths above 1000 nm, the discrepancy between the experiments and the simulations is seen, which was already explained in the previous paragraph.

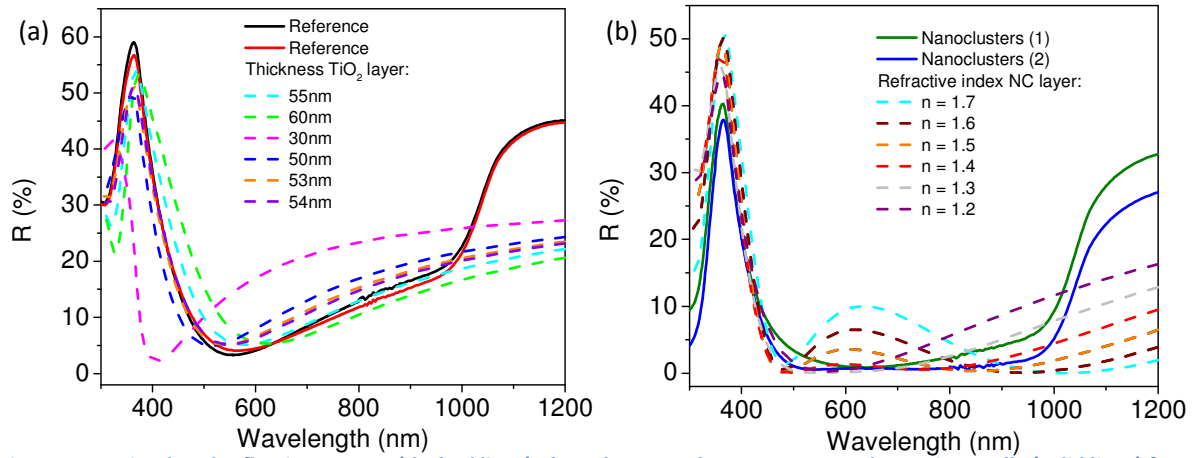


Figure 3.6-2 Simulated reflection spectra (dashed lines) plotted next to the ones measured experimentally (solid lines) for both figures. (a) The thickness of the TiO₂ layer stacked on Si was varied and compared to the experiments to determine the best matching thickness (55nm) and then was used as input for the simulations in figure (b). (b) Simulated reflection spectra with the addition of a dielectric layer, varying its refractive index between 1.2 and 1.7, and this is plotted next to the experimental results.

For completeness, figure 3.6-3 shows the simulations results by convergence testing. The level of error that was introduced by changing the mesh accuracy was first examined and is depicted in Figure 3.6-3 (a). The higher the mesh accuracy, the more accurate the result will be. In general, a mesh accuracy of 4, and 5 yields very accurate results, but requires more computational power. The highest mesh accuracy used in a simulation was 6 and it was used to compare to the simulations with lower mesh accuracies. From 400 to 1200 nm, each simulation showed good agreement with each other (see Table 3.6-1 for the mean error). However, in the range of 300 to 400, the simulated spectra showed some discrepancy between the results. A mean error of ± 1.4 R% in this range was found for the solution with a mesh accuracy of 2, but the accuracy of the result is still good.

Simulations were also checked for convergence versus varying simulation box size. The results are shown in Fig. 3.6-3 (b). Again, better agreement between the solutions was found in the range of 400-1200 nm with respect to the range of 300-400 nm. Overall changing the FDTD size is a lot less prone to giving inaccurate results than changing the mesh accuracy. The mean differences between the different solutions for R% are shown in Table 3.6-2 over 3 different wavelength ranges. It is concluded that changing the geometry of the FDTD, or the mesh accuracy of the simulations for the investigated values, do not give diverging solutions.

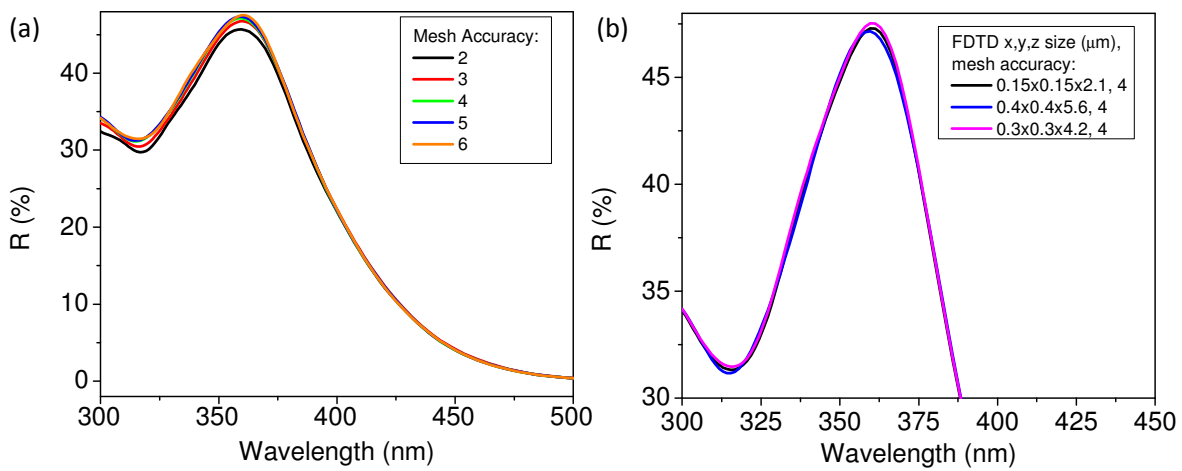


Figure 3.6-3 (a) Convergence testing was done by varying the mesh accuracy between 2 and 6, while keeping other settings constant. (b) The FDTD box size was also changed to study the error.

Mesh accuracy	2 vs 6	3 vs 6	4 vs 6	5 vs 6
Mean error 300-400 nm (R%)	1.350	0.584	0.219	0.195
Mean error 400-1200 nm (R%)	0.025	0.044	0.023	0.020
Mean error 300-1200 nm (R%)	0.469	0.225	0.089	0.079

Table 3.6-1 The mean error in reflectance (R%) is listed for different mesh accuracies for 3 different wavelength ranges. A mesh accuracy of 6 was used as the benchmark for comparing the simulations with lower mesh accuracy.

FDTD size x, y, z (μm)	0.15, 0.15, 2.1 vs 0.4, 0.4, 5.6	0.3, 0.3, 4.2 vs 0.4, 0.4, 5.6
Mean difference 300-400 nm (R%)	0.186	0.039
Mean difference 400-1200 nm (R%)	0.014	0.007
Mean difference 300-1200 nm (R%)	0.072	0.018

Table 3.6-2 The mean difference in reflectance (R%) between simulations where the FDTD geometrical dimensions (x,y,z) have been altered and listed over 3 different wavelength ranges. The mesh accuracy was kept constant at 4.

Calculating the filling fraction - Bruggeman Effective Medium Approximation (BEMA)

Simulation results show that the refractive indices of 1.3 or 1.4 are attributed to the porous TiO₂ layer of NC (region B and A, respectively) the reflection measurements can be reproduced with simulations. We can relate the volume fraction of TiO₂ to the effective refractive index of the porous layer using the Bruggeman effective medium approximation (BEMA) as it is a mixture of materials, which constituents are composed of TiO₂ clusters and voids generally smaller than the wavelength of light²². In this approximation, the following relation holds between the volume fraction of TiO₂ and air, and the indices:

$$f_A \frac{n_A^2 - n_{NC}^2}{n_A^2 + 2n_{NC}^2} + f_B \frac{n_B^2 - n_{NC}^2}{n_B^2 + 2n_{NC}^2} = 0 \quad \text{Equation 3.6-1}$$

With: $f_A + f_B = 1$

and where f_A , n_A , f_B , n_B are the volume fraction (f) and refractive index (n) of TiO₂ (A) and air (B), respectively, and n_{NC} is the effective refractive index of the porous layer. By rearranging the equation, and substituting the following:

$$D = \frac{n_A^2 - n_{NC}^2}{n_A^2 + 2n_{NC}^2}$$

$$E = \frac{n_B^2 - n_{NC}^2}{n_B^2 + 2n_{NC}^2}$$

$$f_B = 1 - f_A$$

A useful equation is derived:

$$f_A = \frac{E}{E - D} \quad \text{Equation 3.6-2}$$

If we insert the known refractive indices of TiO₂ ($n=2.41$ at 1041 nm)¹⁹, air ($n=1$), and the effective refractive index from the simulation results in Equation 3.6-2, we get a $f_A \approx 0.26$ and 0.33 for $n_{NC} = 1.3$ and 1.4 , respectively, which means the porosity is high (0.74 & 0.67). An assumption was made that that the 55 nm thick TiO₂ layer that was evaporated from a TiO₂ source is the same type of amorphous TiO₂ material that was taken from a reference source. In practice, the refractive index has been measured and is shown to be slightly different from the one ($\sim 3\%$) that was used here, and is thus not the exact same TiO₂.²³ It has been shown that the difference in refractive index for the porous layer can be attributed to the difference in volume fraction, i.e. the NC can deposit and pack differently on the surface of TiO₂. It is thought that during deposition, the angle of incidence of the cluster beam relative to the surface may determine the packing, with a higher incidence angle giving a more porous layer.²⁴ Theoretically, this should allow some control over the refractive index of the desired AR coating by optimizing the angle of incidence. It should also be remarked that the NC beam coming out of the nozzle should be thought of as not homogeneous and turbulent, which complicates the understanding of the deposition process.

3.7. Discussion of Results

Depositions of TiO₂ NC have yielded a porous layer on the substrate. Various deposition tries have been done to repeat this, but have yielded poor results believed to be due to some difficulty of sputtering the TiO₂ material. Although the desired size of clusters on the order required for Mie scattering was not produced (100 nm height, 350 diameter, average pitch of 500 nm)²⁵, it is still possible to attempt to deposit larger cluster sizes by using a higher Ar gas flow, e.g. 40 sccm instead of the 15 sccm that was used here, but is outside the operating range of the experimental set-up. Adding an oxygen flow alongside argon might also be interesting to observe any cluster size changes. AFM and SEM imaging showed that the deposited layer of the sample of interest showed large variation in height. We also consistently see that the antireflection effect is not attributed to Mie scattering into the wafer, 1) as the individual clusters are significantly smaller than the wavelength of light as seen in the SEM micrograph, 2) experimental and simulations show that the reflection spectra of the TiO₂ NC do not have a first-order Mie resonance in the spectral range of 500-800nm²⁶, 3) The transmission spectra did not show any decreased transmission.

The experimental and simulation of the reflection spectra agree well on the type of AR coating that is the case here, which is a graded index of layers consisting of a low index layer on top, and an increasing index with each underlying layer. The same results also show that the configuration that was made can achieve a low reflection of 5.7% over a broadband spectral range. Qualitatively, the porosities that are derived from the filling fraction of TiO₂ using the BEMA agrees with the result of the SEM micrograph – a large fraction of void volume are seen between the loose connected network of clusters, although this could not be determined due to the difficulty in counting the clusters that are hidden from view due to stacked columns of clusters. In accordance with optical microscopy, SEM also demonstrates that the layer itself is homogeneous.

Parasitic light absorption by TiO₂ is expected to be present in the spectral range below 400 nm²⁷. This study did however not account for the light absorption in the NC. If these NC are treated as a bulk material, i.e. the equivalent layer would be a thin layer as if all the clusters would be “squeezed” into a homogeneous layer, then the combined thickness would still have a low parasitic light absorption. More study regarding the light absorption characteristics of the NC is required. It is not exactly clear how two different regions with two different porosities for the NC layer were created, although it is speculated that the angle of incidence and the inhomogeneity of the cluster beam may play a role. Using the nanocluster source, a new method was found to create a low index porous TiO₂ layer that can be used in an AR coating configuration. Any change of the lifetime for the minority charge carriers should be further investigated by including a passivation layer (Al₂O₃) on the Si wafer, and deposition of the NC. Even though this AR coating was not tested in a real solar cell configuration, it is still a promising idea that could improve the performance of solar cells, but that will need more research to determine 1) the open-circuit voltage, and 2) the short-circuit current.

4. Conclusions

The attempt to create the Mie AR coating using the nanocluster source did not succeed with the explored parameters (current/voltage, Ar gas flow and aggregation length). Optical microscopy showed that the deposited layer of interest is homogeneous. SEM demonstrated that this layer is porous and consists of a loose network of nanoclusters with rather uniform sizes of about 20-25 nm. An alternative AR coating was made that relies on a graded index of stacked layers, with the upper layer turning out to be a porous TiO₂ material with a low effective refractive index of about 1.3 and 1.4 depending on the porosity. This was validated using a combination of FDTD simulations and UV-Vis-NIR spectroscopy, with the measured reflection spectra showing that a broadband reflection of 2.3% was realized, which achieves the same level of reflection with the Mie coating of nanopillars. No decrease in transmission with the porous layer compared to the reference was measured however. More investigation is needed into the passivation properties of this alternative AR coating and the light absorption of the nanoclusters in order to give an assessment of the performance in such a proposed solar cell configuration. This research provides insight to a new method to create an AR coating with a very low broadband reflection.

Acknowledgements

This thesis could not have been written without the close support of other people. Firstly, I would like to thank Marcel Di Vece for letting me use the nanocluster source setup again, for introducing me this project, providing other means for the project, but also for our useful discussions and answering my questions. I learned a lot of from our collaboration. I am very grateful to Frank Lenzmann who too, made this internship project possible. Our weekly meetings provided ideas and feedback, essential to the project. I wish your health all the best! Thank you, Pierpaolo Spinelli, your suggestions and tips led me to explore FDTD simulations, and being there as a supervisor was also important to getting the project finished. Working on a project can never be lonely if you have someone to work experiments together with. I enjoyed our collaboration and discussions, George Giannakoudakis. Making sure the depositions were running smoothly, getting the nicest AFM micrograph possible, and finding our way on how to use the UV-Vis-NIR spectrometer was at times not as simple as we wanted! I am indebted to Tim Veldhoven at ECN for spending so much time preparing the SALSA set-up for doing TiO₂ sputtering on crystalline wafers, and helping me with UV-Vis measurements. Good luck on your PhD defence.

My thanks also go out to Marcel Bregman at ECN, who used his expertise to measure SEM micrographs. For explaining on how to operate the UV-Vis-NIR spectrometer, thank you, Klaas Bakker. Your explanation about the optical microscope was very informative, Erik Schuring, thank you too. Much thanks for teaching me about Lumerical FDTD solutions, Thomas, it was very useful.

A last thanks to the wonderful people I could meet working at the Ornsteinlab, ECN in Petten, and my family for supporting me.

References

- ¹ Bruno Burger et al., *Photovoltaics Report*, p.4 website: www.ise.fraunhofer.de (24 October 2014)
- ² P. Spinelli, *Light trapping in solar cells using resonant nanostructures*, Ph.D Thesis University of Amsterdam, p.12 (December 2013)
- ³ D. H. Neuhaus, A. Münzer, *Review Article: Industrial Silicon Wafer Solar Cells*, *Advances in OptoElectronics* **2007**, p.11 (2007)
- ⁴ P. Spinelli, *Light trapping in solar cells using resonant nanostructures*, Ph.D Thesis University of Amsterdam, p.1, 73, 99 (December 2013)
- ⁵ P. Spinelli et al, *Al₂O₃/TiO₂ nano-pattern antireflection coating with ultralow surface recombination*, *APPLIED PHYSICS LETTERS* **102**, P.1 2013
- ⁶ Image taken from: <http://pag.lbl.gov/Research-Topics/newsitem1> visited on 8-1-2015
- ⁷ *Magnetron Sputtering Technology*, pdf taken from: <http://www.directvacuum.com> visited on 2-2-2015, p. 1-2
- ⁸ Nanocluster Solutions brochure, *Metallic, semiconducting and magnetic clusters – Compound clusters*, taken from www.oaresearch.co.uk on 2-2-2015, p. 2
- ⁹ W. Tang, *Si Quantum Dots for Solar Cells*, Master's Natural Science Thesis in Energy Science, University Utrecht, p. 16 (2014).
- ¹⁰ Figure 8 from test data for the NC200U obtained from: <http://www.oaresearch.co.uk> visited 2-2-2015
- ¹¹ R. A. Wilson, H. A. Bullen, *Introduction to Scanning Probe Microscopy (SPM) Basic Theory Atomic Force Microscopy (AFM)*, obtained from: <http://asplib.org> on 2-2-2015, p. 2,3,5,7
- ¹² W. Tang, *Si Quantum Dots for Solar Cells*, Master's Natural Science Thesis in Energy Science, University Utrecht, p. 25 (2014).
- ¹³ B. Hafner, *Scanning Electron Microscopy Primer*, obtained from: <http://www.charfac.umn.edu/> visited on 2-2-2015, p. 1,3,5 (2007)
- ¹⁴ English brochure of SU-70, obtained from: www.hht-eu.com/ visited on 2-2-2015, p. 10 (2010)
- ¹⁵ DRA 4000, 5000 and 6000i document obtained from: <http://mmrc.caltech.edu> visited on 2-2-2015, p. 3-5
- ¹⁶ *FDTD Solutions Numerical Methods*, slides in PDF form obtained from: <https://www.lumerical.com/> visited on 2-2-2015, p.8 (2012)
- ¹⁷ Information page of FDTD found on: <http://www.remcom.com/> visited on 2-2-2015, (2014)

¹⁸ <https://www.lumerical.com/>

¹⁹ J. R. DeVore, *Refractive Index of Rutile and Sphalerite*, J. Opt. Soc. Am. **41**, p. 416-419 (1951).

²⁰ P. Spinelli et. al, *Al₂O₃/TiO₂ nano-pattern antireflection coating with ultralow surface recombination*, APPLIED PHYSICS LETTERS **102**, P.1 2013

²¹ P. Spinelli, *Light trapping in solar cells using resonant nanostructures*, Ph.D Thesis University of Amsterdam, p.97 (December 2013)

²² K. Kulathuraan, P. Jeyakumar, N. Prithivikumaran and B. Natarajan, *Effect of Polymer Fraction on Refractive Index of Nanocrystalline Porous Silicon*, Journal of Applied Sciences, **12**, p. 1671-1675 (2012).

²³ P. Spinelli, *Light trapping in solar cells using resonant nanostructures*, Ph.D Thesis University of Amsterdam, inset (A) of figure 9.4 (b), p.97 (December 2013)

²⁴ X. Fu et al., *ZrO₂ films with variable refractive index by glancing angle deposition*, Chinese Optics Letters **4**, p. 248 (2006)

²⁵ P. Spinelli et al, *Al₂O₃/TiO₂ nano-pattern antireflection coating with ultralow surface recombination*, APPLIED PHYSICS LETTERS **102**, P.1 2013

²⁶ P. Spinelli, *Light trapping in solar cells using resonant nanostructures*, Ph.D Thesis University of Amsterdam, inset (A) of figure 9.4 (b), p.99 (December 2013)

²⁷ P. Spinelli, *Light trapping in solar cells using resonant nanostructures*, Ph.D Thesis University of Amsterdam, inset (A) of figure 9.4 (b), p.106 (December 2013)